Oxid Met (2010) 73:531–550
DOI 10.1007/s11085-010-9191-9

ORIGINAL PAPER

High Temperature Oxidation Behaviour of Nanostructured Alumina–Titania APS Coatings

A. Rico · J. Rodríguez · E. Otero

Received: 3 August 2009 / Revised: 8 October 2009 / Published online: 10 February 2010

Abstract Isothermal oxidation tests at 400, 500 and 600 °C were performed on nanostructured and conventional alumina–titania coatings at different exposure times in air environment. Although parabolic kinetics were observed for most of the experimental conditions, a transition between parabolic and quasi-linear kinetics was found for the conventional system at very demanding conditions (high temperature and exposure time). The better crack propagation resistance of the nanocoating, due to its particular hierarchical microstructure, is thought to be responsible for the enhanced behaviour and the better oxidation resistance observed in this coating.

Keywords Ceramic coating · Nanostructure · Oxidation behaviour · Alumina–titania

Introduction

Ceramic coatings are used in applications where good tribological properties, elevated hardness and high thermal and corrosion resistance are required. Coatings based on alumina are a good alternative when wear resistance and chemical stability are the controlling factor. Alumina is hard but its main drawback is its brittleness [1–3]. The addition of titanium oxide leads to a balanced equilibrium of properties maintaining enough hardness and increasing considerably the coating toughness. Titanium oxide has a lower melting point and plays a role of binding alumina grains to achieve coatings with a higher density [4–6].

A. Rico (✉) · J. Rodríguez · E. Otero
Departamento de Ciencia e Ingeniería de Materiales, Universidad Rey Juan Carlos, C/Tulipán S/N 28933, Móstoles, Madrid, Spain
e-mail: alvaro.rico@urjc.es

These coatings are usually applied by a thermal spray process because a very high temperature is required to melt the ceramic powder. Atmospheric plasma spray is one of the most commonly used techniques because in comparison to other thermal methods such as flame spraying, it provides coatings with better quality, good adherence to the substrate and a lower level of porosity. Great efforts have been made to evaluate the dependency of the behaviour of the coating on the atmospheric plasma projection parameters [1, 6, 7].

During the last years, enhanced mechanical properties in bulk materials and coatings with nano-scale microstructures have been reported, leading to a growing interest in the study and analysis of this type of materials [7–14]. Plasma sprayed alumina–titania coatings have also been prepared from nanocrystalline powders. Two main difficulties should be confronted during the coatings manufacturing: the small size of the nanoparticles impedes the direct projection in conventional plasma equipments and the elevated temperatures presumably reached in the plasma jet may destroy the original nanostructure during thermal spraying if the process is not carefully controlled [7, 9]. To circumvent the first of these obstacles an agglomeration process, previously developed by Gell and co-workers [7–11] and patented by INFRAMAT ADVANCED MATERIALS^{TM}, can be used to prepare agglomerates of nanoparticles by spray drying with average sizes similar to those of the conventional powders (approximately 30–50 μm). These agglomerates can be projected using standard plasma equipments [15]. On the other hand, the nanostructure is maintained if the temperature during plasma spraying is set up at intermediate values between the melting points of alumina and titania. An absolute control of the atmospheric plasma projection parameters is needed and modifying the so called CPSP parameter (Intensity * Voltage/Gas flow) a large variety of micro or nanostructures are attainable [7–14].

Expositions of the coating to high temperature and corrosion environments can produce the coating failure, compromising the mechanical function of the component. Many authors have pointed out that the growing of thermal oxides within the interlayers of the system leads to a complete spallation of the coating, even when mechanical requirements are guaranteed [16]. Durability of ceramic coatings exposed to aggressive environments is related to the morphology and defect distribution of the Thermally Grown Oxides (TGO) formed during the oxidation process. Normally, the failure of the coating is produced when the stresses developed at the interlayer between the ceramic coating and the substrate, by the growing of the TGO, reach a critical value [16].

The specific corrosion products generated at the interlayer are also a key factor controlling the durability of the system. Brittle components like spinels or metallic oxides nucleate cracks faster than other corrosion products. Normally, the generation of brittle oxides is facilitated by an increase in the aggressive gas activity, for example, by increasing the number of cracks in the ceramic top coat. Consequently, to improve the corrosion resistance of the coating an enhancement in the fracture resistance of the ceramic coating is needed.

In this work, the oxidation behaviour of nanostructured and conventional Al_2O_3–13% TiO_2 during the exposition of the coatings to an air environment has been studied. Oxidation kinetics has been determined emphasizing the mechanisms

responsible for the differences achieved between both coatings. Corrosion products have been identified and its influence on the coatings behaviour has been established.

Experimental

Materials

Al_2O_3–13% TiO_2 (wt%) nanostructured and conventional coatings deposited on SAE-42 steel by atmospheric plasma sprayed have been studied. Conventional coatings were fabricated from commercial powder METCO 130 provided by SULZER METCO^{TM}. The average size of the particles is approximately 50 μm in diameter.

Nanostructured Al_2O_3–13% TiO_2 coatings were prepared from agglomerates, supplied by INFRAMAT ADVANCED MATERIALS^{TM}. The agglomerates, constituted by nanometric particles (Nanox^{TM} S2613S) with average size of 200 nm, were prepared by spray drying; being the only difference with the conventional powder the particle size (average diameter of 30 μm). They are able to be projected with standard APS equipments.

In both cases, a Ni–Al–Mo 90/5/5 (wt%) bond coat was projected between substrate and ceramic coating to enhance the adherence of the ceramic layer.

The final coatings present thicknesses of approximately 600 μm including the bond coat. The parameters controlling the APS process were the same for both types of coatings and they are indicated in Table 1.

Experimental Techniques

Oxidation Tests

Isothermal oxidation tests were carried out on conventional and nanostructured coatings. Squared samples (25 × 25 × 5 mm) coated on all its faces were exposed to the oxidative air environment. The oven was preheated to the test temperature before the introduction of the samples. Temperature was stabilized up to ±5 °C respect to the test one and the surface of the sample was adequately prepared by cleaning it using ethanol.

Table 1 APS parameters used to deposit ceramic and bond coats

Parameter/material	Bond coat	Ceramic coatings
Current (A)	120	150
Voltage (V)	80	100
Working gas flow, Ar (SCFH)	40	40
Projection distance (mm)	120	120
Feed powder rate (g min^{-1})	90	80
Incident angle (°)	90	90
CPSP (A·V/SCFH)	–	375

Tests at 400, 500 and 600 °C were developed using different exposure times (24, 100, 150, 200 and 250 h) and a minimum of three tests were performed for each experimental condition. To determine the oxidation kinetics the weight change has been measured by weighting the samples before and after the tests using a precision BP 221 S Sartorius balance.

Scanning and Transmission Electron Microscopy

Initial nanostructured agglomerates were characterized by means of scanning and transmission electron microscopy. With this aim a Philips XL 30 SEM and a Philips Tecnai 20 TEM microscopes were used.

Cross sections of the conventional and nanostructured coatings were prepared from oxidized samples at all experimental conditions to evaluate the microstructural changes generated on the coatings due to the degradation process. Grinding sequence was carried out using SiC papers (600, 1200 and 4000 grit). Afterward, samples were polished in diamond slurry. Observations were made with a JEOL 6400 scanning electron microscopy at high vacuum conditions.

Optical Microscopy

Porosity of nanostructured and conventional coatings was measured by means of a LEICA DMR optical microscope and image analysis software (Image Pro Plus^{TM}). Five images were taken from three different zones of the coatings to evaluate their porosity. Porosity was estimated calculating the ratio between the area occupied by porous and the total area of the image. To make representative this measure, the minimum image size used to calculate this parameter was a square of 50×50 μm^2.

X-Ray Diffraction

X-ray diffraction measurements were also carried out to determine the composition profile through the thickness of the oxidized coating. The samples were polished at 50 μm intervals, afterwards, low angle X-ray diffraction tests were performed on the surface sample at each step. To this end, a Philips PW3040/00 X'Pert diffractometer was used. Main phases formed during oxidation tests at the coating interfaces were determined.

Results

Microstructural Characterization

Nanoparticles Characterization

The agglomerates obtained after spray drying exhibited spherical shape and were formed by irregular shaped and polygonal nanoparticles. TEM observations performed on these particles revealed that they consisted mainly in γ-Al_2O_3 (Fig. 1a)

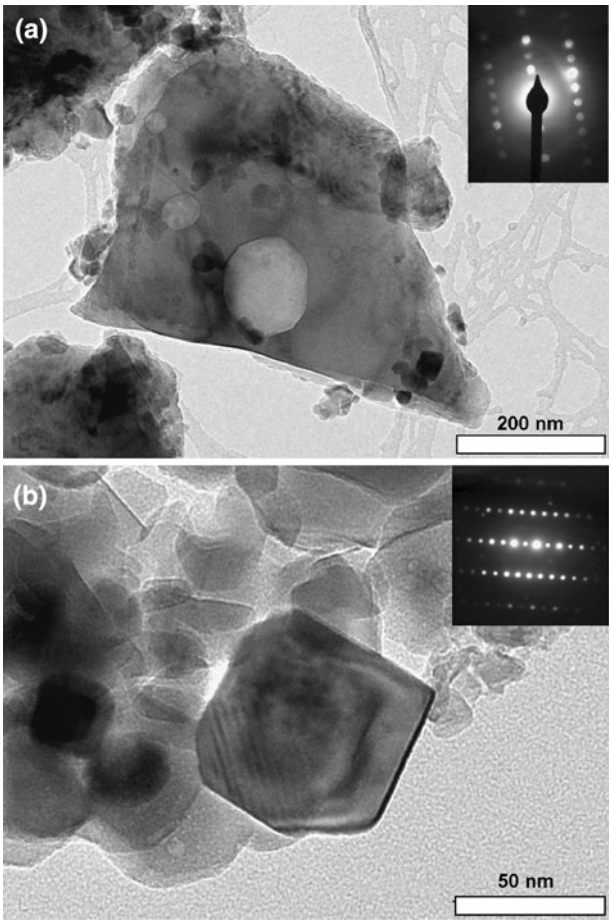

Fig. 1 TEM images showing the nanoparticles composition and morphology. **a** γ-Al_2O_3 nanoparticle showing an EDP with B ⟨1 2 3⟩ orientation. **b** Anatasa nanoparticle showing an EDP with B ⟨2 1 0⟩ orientation

and Anatase-TiO_2 (Fig. 1b). The nanopowders are composed of particles with a bimodal distribution of sizes. Usually, Anatase particles are the smallest ones ranging from 50 to 70 nm, while γ-Al_2O_3 particles present sizes of 200 nm, approximately.

These results are supported by X-ray diffraction experiments carried out on the nanostructured powders. Peaks due to the presence of γ-Al_2O_3 and Anatase are identified in Fig. 2. Additional peaks corresponding to traces of CeO_2 and ZrO_2 can also be observed. These oxides are normally observed when the sol–gel route is used to obtain alumina nanoparticles.

Nanocoating Characterization

Figure 3a shows the cross section of the nanostructured coating. Three layers can be observed. The upper layer is the ceramic coating and the intermediate layer

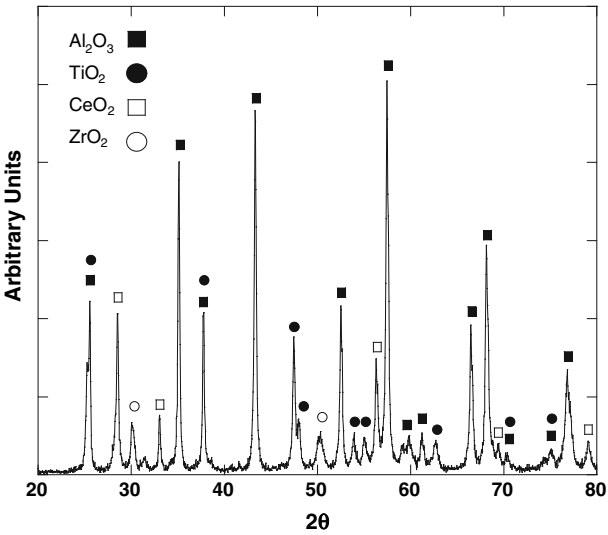

Fig. 2 X-ray diffraction from the nanostructured powders

corresponds to a Ni/Al/Mo bond coat used to minimize the residual stresses due to the mismatch between thermal expansion coefficients of the metallic substrate and the ceramic material. The substrate is made of SAE 42 steel. In Fig. 3b a detail of the ceramic coating is shown. The coating porosity was estimated as 8.7 ± 1.0%. The microstructure of the coating deposited from nanopowders consists of two main zones. Splats formed by deposition of individual molten droplets generate a lamellar fully melted structure (FM) which is typically obtained when thermal projection techniques are used. Nevertheless, partially melted (PM) zones corresponding to the deposition of semi-molten droplets can also be observed in Fig. 3b. To retain the original nanostructure of the feeding agglomerates in the coating, the projection parameters should be selected and controlled with the aim to fix the temperature of the plasma jet between the melting temperatures of both components (γ-Al_2O_3 and TiO_2).

TEM studies developed in the literature [7, 9–11, 13, 14] in similar nanostructured coatings indicated that the FM phases are composed by γ-Al_2O_3. On the other hand, PM zones exhibit a composite microstructure (Fig. 4). The particles observed, with an average size of 200 nm, correspond to the alumina particles previously identified in the nanopowders. However, electron diffraction pattern shown in Fig. 4b indicates that a phase transition occurred during the plasma process. PM zones are essentially composed of α-Al_2O_3, while the primary phase in the powder was γ-Al_2O_3. Although the particles maintain their initial size, they loose the polygonal contour and a smooth and round final shape is observed. The high temperature reached during the projection promotes the phase transition but is not high enough to completely melt the particles. Figure 4c shows that α-Al_2O_3 particles are embedded in a matrix composed by γ-Al_2O_3 nanocrystallites similar to those presented in the FM zones. The only difference is that this matrix is supersaturated in Ti^{4+} because of the formation of a solid solution between the

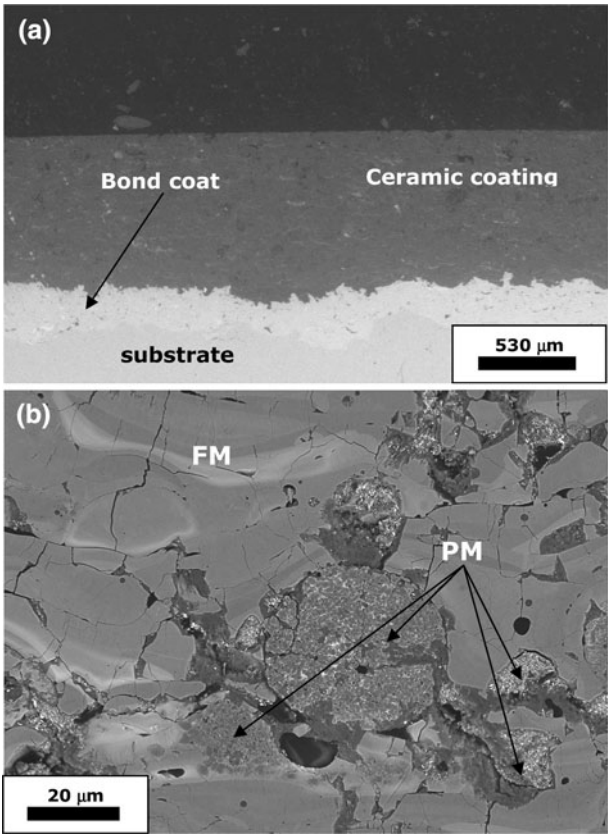

Fig. 3 SEM images showing the nanostructured coating. **a** General. **b** Detail showing a partially melted zone embedded in a fully melted region

γ-Al_2O_3 and the TiO_2 in this zone. These results are in agreement with those obtained in previous works by Shaw et al. [7, 9] and Bansal et al. [13].

Conventional Coating Characterization

Figure 5 shows a SEM micrograph of the conventional coating cross section. The coating porosity was estimated as 11.3 ± 1.4%. The morphology and composition is similar to the FM zones shown in the nanostructured coating. In this case, PM zones are not identified even though projection parameters were identical to those used to deposit the nanostructured coatings. A possible explanation to this phenomenon was given in [11] regarding the morphology of the conventional and nanostructured feeding powders. Unlike METCO-130 powders, comprised of dense particles, the nanopowders are in fact agglomerated particles with a high degree of porosity. Therefore, it is reasonable to expect that the conventional powders exhibited higher heat conduction leading to a better temperature distribution in the plasma jet, which drives to completely melted particles.

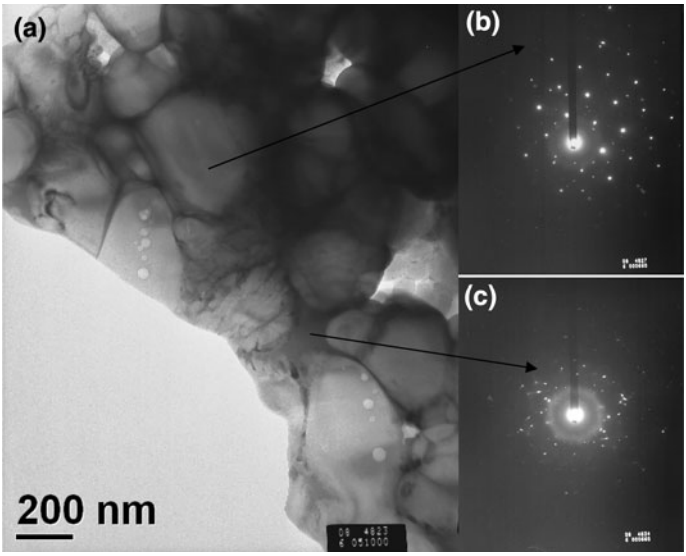

Fig. 4 TEM images showing the morphology and composition of the partially melted zone. **a** Bright field image. **b** EDP corresponding to a α-Al_2O_3 nanoparticle with a B $\langle 1\ 1\ 1 \rangle$ orientation. **c** EDP corresponding to the surrounding matrix

Bond Coat

Figure 6 presents the morphology of the bond coat, which is the same for both coatings. It is composed by Ni crystallites containing aluminium and molybdenum, which were part of the feeding powders composition. In the backscatter contrast, it can be observed dark zones closer to the Ni crystallites (dark zones have been marked with arrows in Fig. 6a).

The TEM analysis has revealed that the Ni present a FCC structure with 200–300 nm in size (Fig. 6b, c). The dark zones, identified previously in the SEM micrograph, have been recognized as γ-Al_2O_3 crystallites as it can be observed in the electron diffraction pattern (EDP) shown in Fig. 6d. This phase was probably formed by the aluminium oxidation during thermal projection. In addition, a granular texture can be appreciated inside the Ni grains. These precipitates probably correspond to γ'-Ni_3Al coherent to the Ni matrix. In Fig. 6c, weak spots, confirming the previous statement can be identified in the EDP under the main spots corresponding to the Ni structure.

Oxidation Kinetics

In Fig. 7a, c, and e the coatings weight change is presented as a function of the oxidation time for the three temperatures used in the oxidation tests. In Fig. 7b, d and f the fits corresponding to a parabolic kinetic are shown for both nanostructured and conventional coatings at 400, 500 and 600 °C. In Table 2 the fitting parameters are collected. The oxygen reaches the bond coat through pores and cracks of the

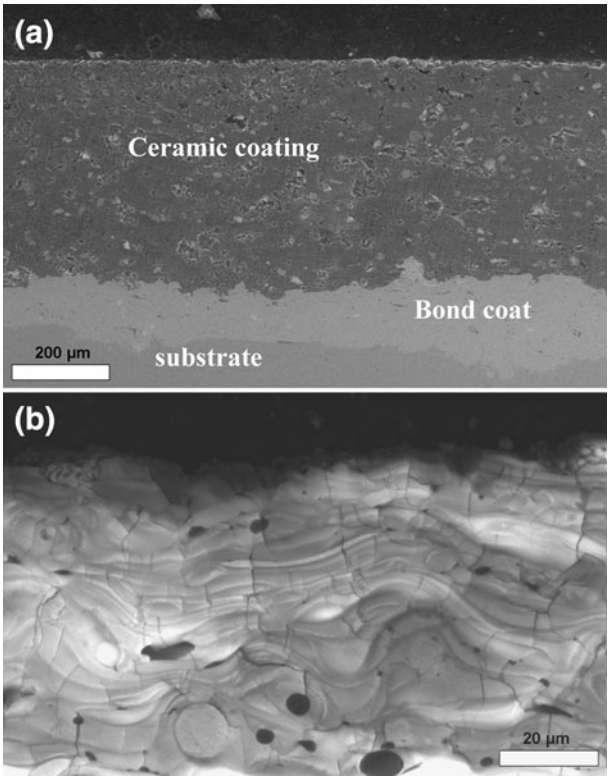

Fig. 5 Cross section of the conventional coating. **a** General. **b** Detail sowing the typical APS coatings splat morphology

ceramic coating, and then, several reactions occurred and fix the oxygen, increasing the mass of the oxidized sample.

In spite of the temperature and exposition time, nanostructured coating presents lower weight change, probably due to the minor porosity exhibited by this coating and due to the presence of Ceria and Zirconia in the nanoparticles composition. As was previously stated, small additions of these two oxides improves the corrosion behaviour of ceramic coatings. The cooperation of these two phenomena drives to minor kinetic constants for the nanocoating, pointing out the major protection offered by the nanostructured system.

Although the behaviour of the two systems is very similar for 400 and 500 °C tests, there is a difference in the tests corresponding to the highest temperature. The nanostructured coating maintains the trend shown at lower temperature, i.e., the kinetics follows a parabolic behaviour. Nevertheless, the conventional coating presents a transition in the oxide kinetics. For times minor than 150 h the kinetic can be expressed in similar terms as that corresponding to lower temperatures, then, the controlling kinetics is parabolic. However, when exposition time is higher than 150 h, the kinetics followed by the system is approximately linear. This transition

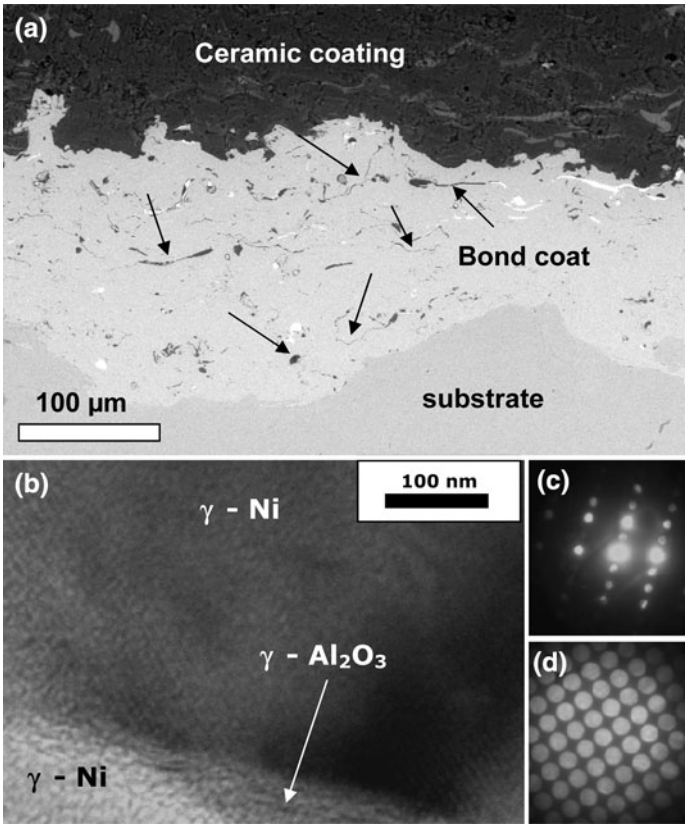

Fig. 6 **a** SEM image showing the bond coat. **b** Bright field image presenting two Ni grains surrounding a γ-Al_2O_3 grain. **c** Ni grain EDP with B $\langle 2\ 1\ 1 \rangle$ orientation. **d** alumina grain EDP with B $\langle 3\ 1\ 1 \rangle$ orientation

points out that at this moment there was not a diffusion barrier impeding the access of oxygen to the metallic components.

In Fig. 8 the kinetics constants estimated from experimental data are fitted using the Arrhenius law (the constant kinetics at 600 °C has been calculated from data corresponding to exposition times lower than 150 h). The results have been collected in Table 2. The activation energy of the overall oxidation process is slightly higher for the nanostructured coating resulting in a better protection than that corresponding to the conventional one.

Cross Sections Analysis

The coatings oxidation behaviour is very similar. The oxidations scales growing in the coating interlayer are comparable in both systems, then the observations presented in the following paragraphs are valid for the two coatings.

In Fig. 9a the cross section of the conventional coating tested at 400 °C during 150 h is presented. It is possible to distinguish two thermally grown oxide scales.

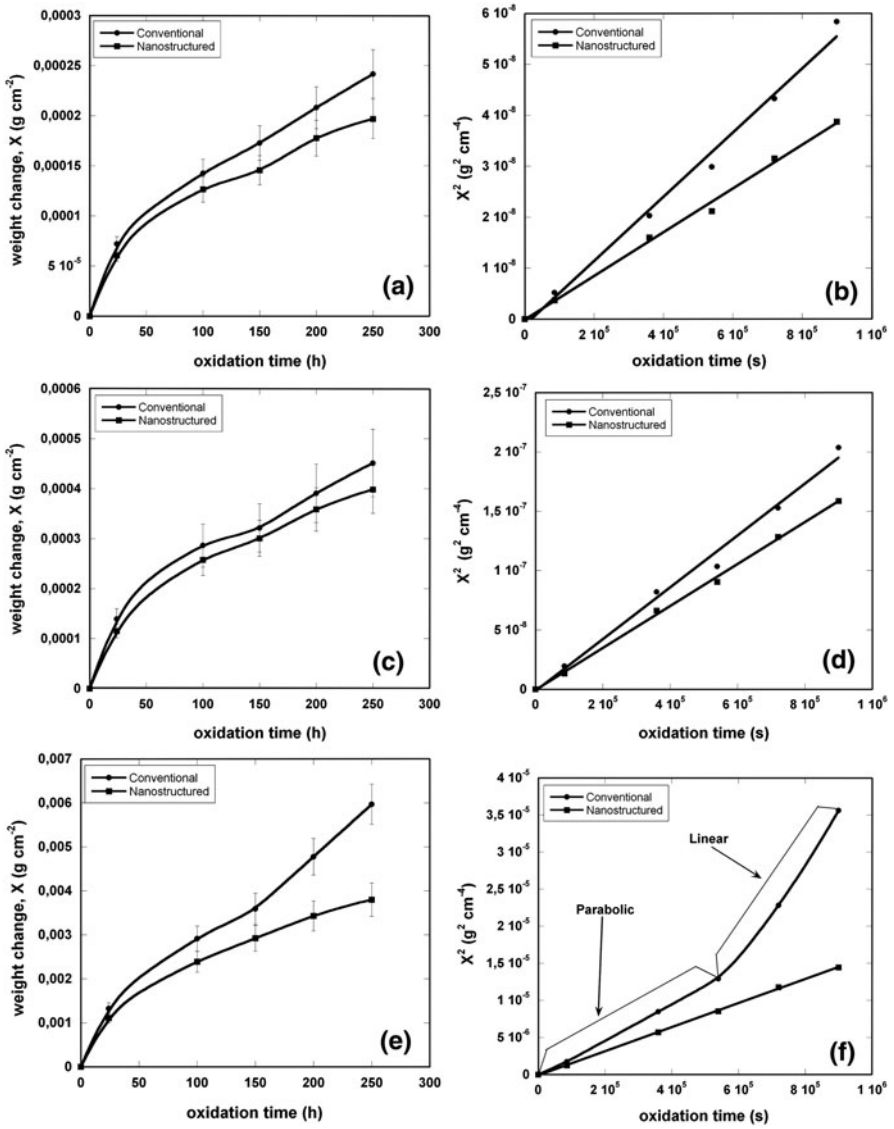

Fig. 7 Weight gain versus oxidation time showing the oxidation kinetics at different temperatures. **a** 400 °C. **b** Parabolic fit for tests performed at 400 °C. **c** 500 °C. **d** Parabolic fit for tests performed at 500 °C. **e** 600 °C. **f** Parabolic fit for tests performed at 600 °C

The first one is discontinuous and is located between the ceramic coating and the bond coat. The second scale grew at the interface between the bond coat and the steel substrate. The oxygen diffuses through the bond coat using the pores and cracks resulting from the thermal projection process, and reaches the substrate. At this temperature there are not big changes in the morphology and composition of the growing oxidation layers.

Table 2 Fitting parameters, constant kinetics and activation energy collected from Figs. 7 and 8

Temperature (°C)	Conventional		Nanostructured	
	K_p (g^2 cm^{-4} s^{-1})	R	K_p (g^2 cm^{-4} s^{-1})	R
400	6.30×10^{-14}	0.99568	4.30×10^{-14}	0.99804
500	2.18×10^{-13}	0.99531	1.76×10^{-13}	0.99209
600 (parabolic)	1.83×10^{-11}	0.99915	1.62×10^{-11}	0.99881
Ea (cal mol^{-1})	13902		14570	

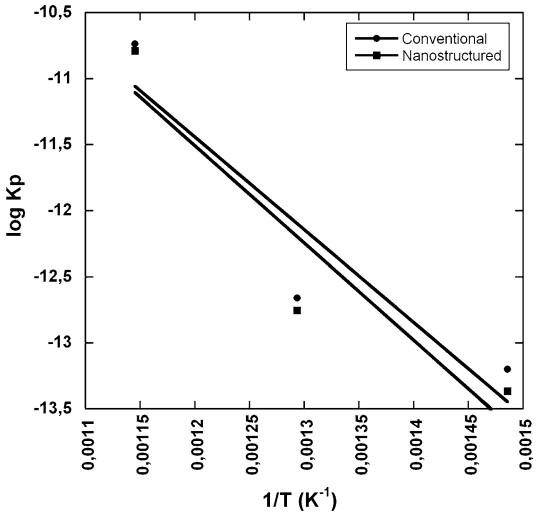

Fig. 8 Arrhenius fit for parabolic constants obtained from Fig. 9

In Fig. 9b, c the cross section of the nanostructured coating tested at 500 °C during 24 and 200 h can be observed, respectively. When exposure times are low, the morphology of the scales are similar to those presented previously corresponding to 400 °C, but there is an important difference, the layer located at the interface between bond and top coats is continuous at this temperature. However, for high exposition times the oxidation layer growing at the Al_2O_3–TiO_2/Bond coat interface presents two subscales. The cross section of the conventional coating tested at 600 °C and low exposure time is shown in Fig. 9d. It is possible to appreciate the presence of continuous scales growing at the interface between the ceramic coating and the bond coat, and between the bond coat and the metallic substrate. In this case the scales are unique. When the exposure time is high (Fig. 9e), it is possible to appreciate that both oxidation layers are composed by two subscales.

In Fig. 9f the conventional coating cross section tested at 600 °C during 250 h is presented. Cracks can be observed emerging from the oxidation products when the thickness of these scales is too big. These cracks can propagate through the ceramic layer and reach the surface (Fig. 9g). The consequence is that the access of oxygen inside the system is facilitated. Nanostructured coating presents the same type of

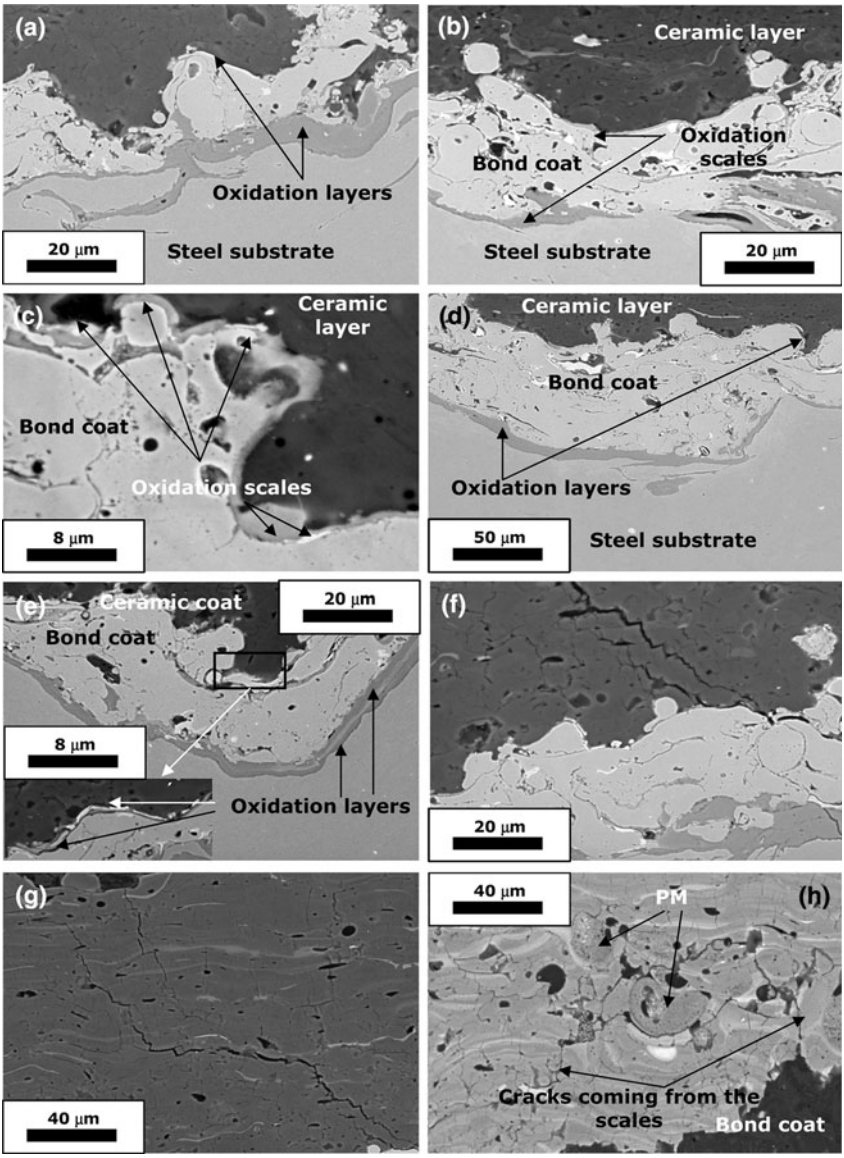

Fig. 9 **a** Cross section of the conventional coating tested at 400 °C after 150 h. Cross section of the nanostructured coating tested at 500 °C. **b** After 24 h. **c** After 200 h. Cross section of the conventional coating tested at 600 °C. **d** After 24 h. **e** After 200 h. Cross section of the conventional coating tested at 600 °C after 250 h. **f** Detail of the crack growing at the TGO layer. **g** The crack reaches the free surface. **h** Cross section of the nanostructured coating tested at 600 °C after 250 h

cracks (Fig. 9h), as well; however, although cracks start its propagation inside the ceramic layer, they do not arrive at the surface. The Partially Melted zones are obstacles arresting and obliging the cracks to deflect around them.

X-Ray Diffraction Analysis

The composition profile carried out on the thickness of the samples indicates which are the oxidation products forming scales during the oxidation at different times and temperatures. Both coatings follow similar trends as was mentioned previously, consequently, next results are referred to the nanostructured coating, although most of the comments are also valid for the conventional one.

In Fig. 10a the evolution of X-ray diffraction spectra taken from the interlayer zone between the ceramic coating and the bond coat (interface 1) after 100 h is shown at different temperatures. At 400 °C, α-Al_2O_3, is the main component detected in the scale. Signals from Ni and γ'-Ni_3Al coming from the bond coat grains can be also observed. At 500 °C, the composition of the different layers is very similar to that from minor temperatures. Thus, the main phases forming the scale are α-Al_2O_3 too. At 600 °C the spinel $NiAl_2O_4$ appears as the unique corrosion product, while in this case, α-Al_2O_3 does not form. This fact show that the spinel forms directly from the Ni–Al alloy in the bond coat.

Figure 10b presents X-ray diffraction spectra taken from the interlayer zone between the bond coat and the substrate (interface 2) after 100 h at different temperatures. When the oxidation time is low, the main corrosion product is the spinel $NiFe_2O_4$, in spite of the test temperature.

In Fig. 11a X-ray diffraction spectra taken from the interface 1 after 200 h is shown at different temperatures. At 400 °C, the composition of this scale is very similar to that observed at lower exposure times. However, when oxidation tests are carried out at 500 °C it is formed not only by α-Al_2O_3, but also by $NiAl_2O_4$. In the spectra of samples tested at 600 °C peaks corresponding to $NiAl_2O_4$ and to NiO can

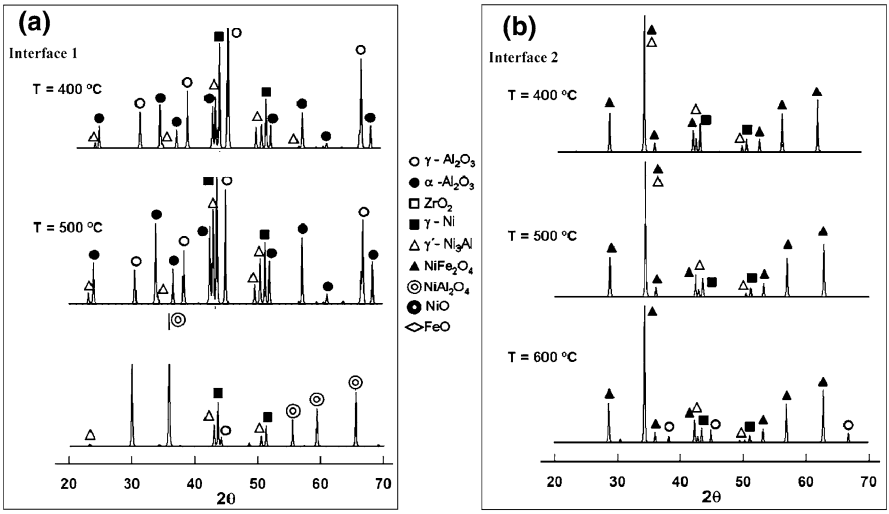

Fig. 10 X-ray diffraction spectra for nanostructured samples tested at different temperatures after 100 h. **a** Taken from the interlayer region between ceramic top coat and bond coat. **b** Taken from the interlayer region between bond coat and substrate

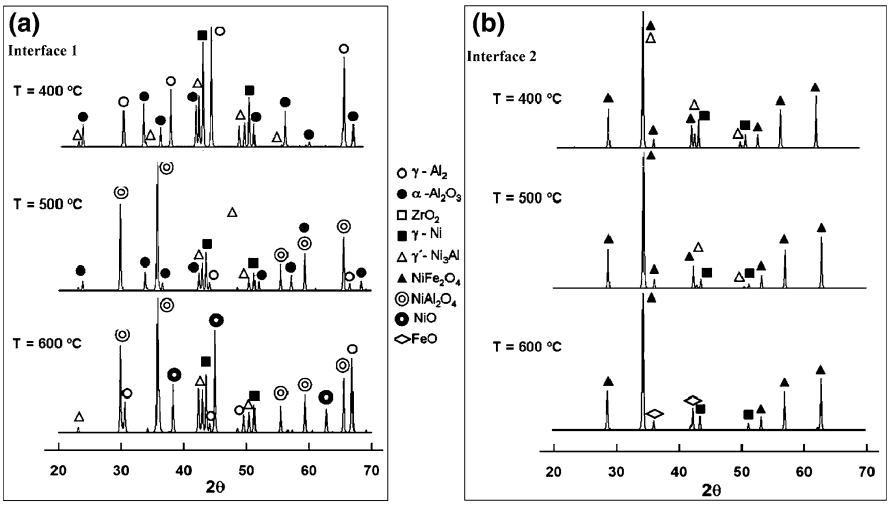

Fig. 11 X-ray diffraction spectra for nanostructured samples tested at different temperatures after 200 h. **a** Taken from the interlayer region between ceramic top coat and bond coat. **b** Taken from the interlayer region between bond coat and substrate

be identified. It is interesting that the NiO cannot be observed in the nanostructured coating up to 250 h of exposition, while the conventional material exhibits this component after only 200 h.

Figure 11b shows X-ray diffraction spectra taken from interface 2 after 200 h at different temperatures. When the exposure time is high, the spectra corresponding to tests performed at 400 and 500 °C include $NiFe_2O_4$ as the main corrosion product. In contrast, this scale presents a dual composition when tests are carried out at 600 °C. Peaks related to $NiFe_2O_4$ and FeO can be observed in the X-ray spectrum.

Finally, to clarify the overall oxidation process, in Fig. 12 a schematic view of the different layers which form during the oxidation at different times and temperatures is shown.

Discussion

From the experimental results it can be concluded that the oxidation kinetics follows a parabolic law for the majority of the experimental conditions. Although the corrosion products are deposited on two zones, the overall degradation process can be explained in terms of a parabolic oxidation law as a result of the superposition of two growing scales. Therefore, the oxide growth is controlled by the ions diffusion or the electron transport through the physical barriers up to reach the metallic material. Firstly, they have to diffuse through the ceramic layer, afterwards, they have to cross the oxide scale generated during the initial stages of the oxidation process, as well.

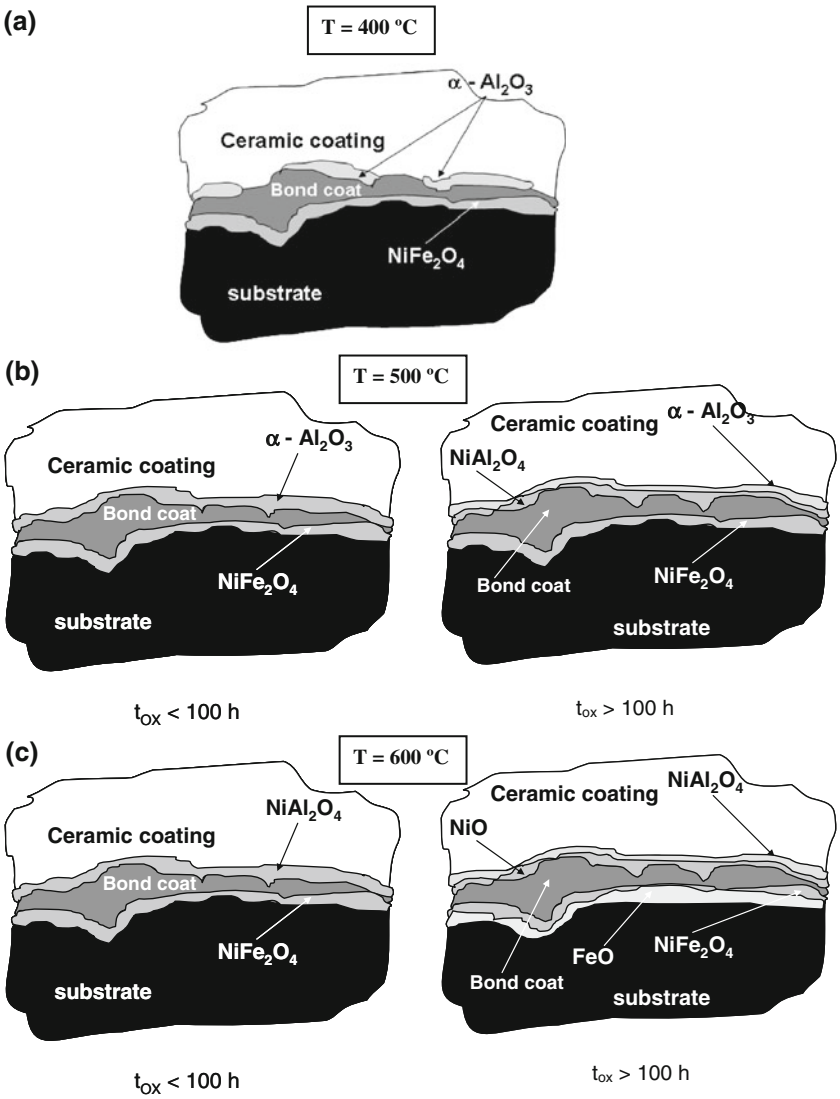

Fig. 12 Schema showing the different scales generated during the oxidation tests. Test temperature of **a** 400 °C, **b** 500 °C, **c** 600 °C

However, there is a remaining question arising from the kinetics results. The oxidation kinetics show a transition between parabolic and linear laws when the conventional coating is tested at 600 °C. This transition is not observed for the nanocoating. This enhanced behaviour has to be addressed to the microstructural and morphology differences between materials. Initially, the ceramic coating plays a passive role as a physical barrier impeding the access of oxygen to the bond coat. Then, the PM zones promote an active protection mechanism which improves the

oxidation resistance of the coating. If the thickness of the scales generated from the deposition of the corrosion products at the system interlayer reaches a critical value, the high stresses achieved at these zones initiate cracks from the oxidation layers. Figure 9f, g point out that, in the conventional coating, the cracks propagate through the ceramic top layer and reach the free surface. Thus, the direct access of oxygen to the metallic components is granted. It is at this moment when the transition in the kinetics occurred. Nevertheless, although similar cracks are created in the nanostructured coatings (Fig. 9h) the partially melted zones work as reinforcements of the ceramic matrix increasing the toughness of the coating. In fact, it can be observed crack deflection phenomena around these PM particles. As a consequence is more difficult that cracks reach the surface of the nanostructured material, and then, the top coat remains as an effective physical barrier, increasing the protection against oxidation compared to the conventional one.

The oxidation behaviour and the corrosion products are similar for both coatings, although, probably due to the minor porosity, the formation of some of them is slightly delayed in the nanostructured material. Therefore, a common discussion will be performed.

The formation of corrosion products can be explained considering the activity of the main bond coat components with oxygen. Stiger et al. [17] studied the stability regions for multiple corrosion products generated in the Ni–Al–O system (Fig. 13). The component showing the highest activity is aluminium and, normally, this will be the first component reacting with oxygen. As it is consumed, forming different oxidized aluminium species, its activity decreases, rising, then, the Ni activity. Therefore, as the aluminium disappeared, oxidized nickel species will start to form. In addition, local ruptures or cracking could favour the oxygen activity at the metallic interface and the nickel oxidation.

At 400 °C, the scale growing at the interface 1 is discontinuous, and it is formed by α-Al_2O_3. In this case, the corrosion product appears from direct oxidation of the

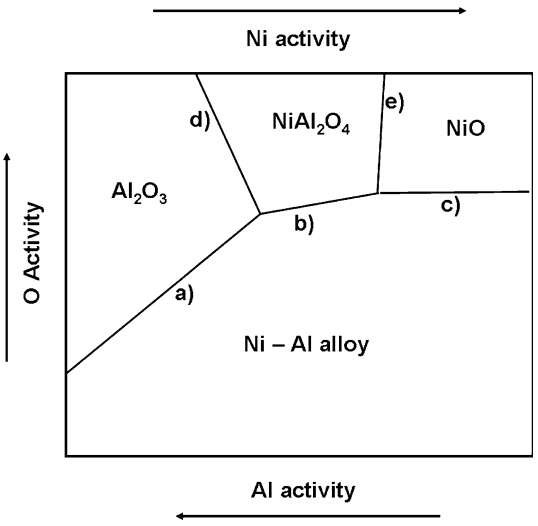

Fig. 13 Diagram showing the stability fields depending on the components activity for the different phases that can be obtained from the system Ni–Al–O

aluminium included in the metallic alloy, following the equilibrium line (a) at the diagram shown in Fig. 13 [17]:

$$2\mathrm{Al(Alloy)} + 3\mathrm{O} \leftrightarrow \mathrm{Al_2O_3} \quad (1)$$

The scale closer to the substrate is composed mainly by the spinel $NiFe_2O_4$. Its presence, instead of Ni–Al spinels, indicates that the aluminium contained in the bond coat diffuses to the upper interlayer to react with oxygen. When it is almost consumed, the oxygen is transported through the bond layer up to the interface 2, generating the Ni–Fe spinel. These observations are maintained for all exposure times.

As the temperature increases, the scale located at the interface 1 becomes continuous. Nonetheless, its composition and morphology depend on the oxidation time. At low exposition time the situation described previously at 400 °C is reproduced. In contrast, when the time is elevated, the formation of Ni–Al spinels is activated and $NiAl_2O_4$ can be easily detected in the composition analysis. However, the scale is formed by two sublayers because of the formation of α-Al_2O_3 at the initial oxidation stages. The spinel can be formed from two alternative reactions, depending on the (b) and (d) equilibriums lines collected in Fig. 13 [17]:

$$\mathrm{Ni(Alloy)} + 2\mathrm{Al(Alloy)} + 4\mathrm{O} \leftrightarrow \mathrm{NiAl_2O_4} \quad (2)$$

$$3\mathrm{Ni(Alloy)} + 4\mathrm{Al_2O_3} \leftrightarrow 3\mathrm{NiAl_2O_4} + 2\mathrm{Al(Alloy)} \quad (3)$$

There is no change on the scale growing at the interface 2, except of the increase in thickness, being the main corrosion product the $NiFe_2O_4$ spinel.

The superior scale is composed by $NiAl_2O_4$ when the oxidation test is performed at 600 °C. For these conditions, the oxygen activity is high enough to place the system at the d equilibrium line in Fig. 13. This means that the spinel can be formed directly from the metallic alloy, following reaction (2). Nevertheless, if exposure time increases, the aluminium is totally consumed, promoting the nickel activity to rise. Therefore, the formation of NiO is obtained. This component can be created from two reactions, controlled by the c and e equilibriums in Fig. 13 [17]:

$$\mathrm{Ni(Alloy)} + \mathrm{O} \leftrightarrow \mathrm{NiO} \quad (4)$$

$$3\mathrm{Ni(Alloy)} + \mathrm{NiAl_2O_4} \leftrightarrow 4\mathrm{NiO} + 2\mathrm{Al(Alloy)} \quad (5)$$

The last component formed constitutes the subscale closer to the bond coat, while the first one is placed near to the ceramic coating. Thus, a dual morphology can be appreciated in the thermally grown oxide at these conditions (Fig. 9e).

There exists a delay for the formation of NiO in the nanostructured coating. This phenomenon can be explained in terms of the cracking processes occurring at the very demanding conditions described before. In the conventional coating, cracks allow the oxygen accessing easily to the metallic components, increasing rapidly the oxygen activity. In the nanostructured coating, on the contrary, cracks do not reach the surface and the oxygen activity remains low at the same conditions. In this material more time is needed to achieve an oxygen activity high enough to let the formation of NiO.

A scale, mainly formed by $NiFe_2O_4$, is obtained at low times at the interface 2. Afterwards, for longer times the nickel is totally consumed near the interface and

the formation of other oxidized components, such as iron oxides, is promoted. Dual scales are observed in samples tested at 600 °C. The first subscale formed near to the bond coat is $NiFe_2O_4$ and the subscale created later close to the substrate is FeO.

Many authors have pointed out that the formation of NiO or FeO is a signal of the component failure [16]. These are brittle products, where cracks can be generated. This work demonstrates the better oxidation behaviour of the nanostructured coating, as a result of its crack propagation resistance due to the presence of the partially melted zones. The increasing in fracture toughness, compared to the conventional coating, allow extending the working life of the component when the nanosystem is used.

Conclusions

Microstructural and high temperature corrosion behaviour of nanostructured ceramic Al_2O_3–13% TiO_2 coatings has been analyzed. In terms of comparison, conventional coatings used nowadays in the industry were also studied. From results, the following conclusions can be drawn:

- Atmospheric plasma spraying has been used successfully as deposition technique to manufacture nanostructured coatings of alumina–titania. A hierarchical microstructure can be obtained if the spraying parameters are controlled carefully. This microstructure can be modelled as a ceramic matrix composite, where the matrix is composed by γ-Al_2O_3 (fully melted zones, FM) and the reinforcement shows a composite structure as well: α-Al_2O_3 nanoparticles surrounded by a supersaturated Ti^{4+} γ-Al_2O_3 matrix. This microstructure is the so called partially melted zone (PM). Conventional coating is composed totally by a morphology equivalent to the fully melted zones, i.e., splats constituted by supersaturated Ti^{4+} γ-Al_2O_3 are obtained from spraying micrometric feeding powders.
- The overall oxidation process follows a parabolic kinetics, then, the ions transition through the diffusion barriers of the system (ceramic coating, TGO's, etc.) seems to be the oxidation mechanism controlling factor. The lower porosity exhibited by the nanocoating and the presence of Ceria and Zircona in its composition are thought to be the main reasons explaining the minor kinetics shown by the nanostructured material.
- The oxidation products and the scales morphology depend on oxidation temperature and time. Two oxidation layers can be observed in the environmental barrier system. The first one grows between the ceramic top coat and the bond coat; and the main corrosion products are α-Al_2O_3 and $NiAl_2O_4$. The second layer is located at the interface between the bond coat and the substrate and it is mainly formed by the $NiFe_2O_4$ spinel. Even FeO can be finally obtained.
- When oxidation conditions are highly demanding cracks are generated at the system interlayer. In the conventional material the cracks reach the free surface, and allow the oxygen accessing directly to the metallic components. As a consequence, a transition between parabolic and quasi-linear kinetic laws is produced. The partially melted zones embedded in the nanocoating microstructure are able to arrest and deflect the cracks, avoiding the direct access of

oxygen. Thus, the parabolic law is maintained for all the experimental conditions. As a consequence, oxidation resistance offered by the nanocoating is higher to that presented by the conventional material.

Acknowledgment The authors wish to thank Comunidad de Madrid for the financial support through program ESTRUMAT and Grant no. 5863.

References

1. P. V. Ananthapadmanabhan, T. K. Thiyagarajan, R. U. Satpute, N. Venkatramani, and K. Ramachandran, *Surface and Coatings Technology* **168**, 231 (2003).
2. K. Ramachandran, V. Selvarajan, P. V. Ananthapadmanabhan, and K. P. Sreekumar, *Thin Solid Films* **315**, 144 (1998).
3. L. C. Erickson, H. M. Hawthorne, and T. Troczynski, *Wear* **250**, 569 (2001).
4. D. I. Pantelis, P. Psyllaki, and N. Alexopoulos, *Wear* **237**, 197 (2000).
5. S. Gessasma, M. Bounazef, P. Nardin, and T. Sahraoui, *Ceramics International* **32**, 13 (2006).
6. B. Normand, V. Fervel, C. Coddet, and V. Nikitine, *Surface and Coatings Technology* **123**, 278 (2000).
7. L. L. Shaw, D. Goberman, R. Ren, M. Gell, S. Jiang, Y. Wang, T. D. Xiao, and P. R. Strutt, *Surface and Coatings Technology* **130**, 1 (2000).
8. Y. Wang, S. Jiang, M. Wang, S. Wang, T. D. Xiao, and P. R. Strutt, *Wear* **237**, 176 (2000).
9. M. Gell, E. H. Jordan, Y. H. Sohn, L. Shaw, and T. D. Xiao, *Surface and Coatings Technology* **146–147**, 48 (2001).
10. E. H. Jordan, M. Gell, Y. H. Sohn, D. Goberman, L. Shaw, S. Jiang, M. Wang, T. D. Xiao, Y. Wang, and P. Strutt, *Materials Science and Engineering* **A301**, 80 (2001).
11. D. Goberman, Y. H. Sohn, L. Shaw, E. Jordan, and M. Gell, *Acta Materialia* **50**, 1141 (2002).
12. Y. Liu, E. T. Fischer, and A. Dent, *Surface and Coatings Technology* **167**, 68 (2003).
13. P. Bansal, N. P. Padture, and A. Vasiliev, *Acta Materialia* **51**, 2959 (2003).
14. X. Lin, Y. Zeng, S. W. Lee, and C. Ding, *Journal of the European Ceramic Society* **24**, 627 (2004).
15. X. Q. Cao, R. Vassen, S. Schwartz, W. Jungen, F. Tietz, and D. Stöever, *Journal of the European Ceramic Society* **20**, 2433 (2000).
16. A. G. Evans, D. R. Mumm, J. W. Hutchinson, G. H. Meier, and F. S. Pettit, *Progress in Material Science* **46**, 505 (2001).
17. M. J. Stiger, N. M. Yanar, M. G. Topping, F. S. Pettit, and G. H. Meier, *Zeitschrift fur Metallkunde* **90**, 1069 (1999).